

AperTO - Archivio Istituzionale Open Access dell'Università di Torino

Micro-beam and pulsed laser beam techniques for the micro-fabrication of diamond surface and bulk structures

This is the author's manuscript

Original Citation:

Availability:

This version is available <http://hdl.handle.net/2318/1509398> since 2018-01-18T13:52:34Z

Published version:

DOI:10.1016/j.nimb.2014.11.061

Terms of use:

Open Access

Anyone can freely access the full text of works made available as "Open Access". Works made available under a Creative Commons license can be used according to the terms and conditions of said license. Use of all other works requires consent of the right holder (author or publisher) if not exempted from copyright protection by the applicable law.

(Article begins on next page)



UNIVERSITÀ DEGLI STUDI DI TORINO

This is an author version of the contribution published on:

Questa è la versione dell'autore dell'opera:

“Micro-beam and pulsed laser beam techniques for the micro-fabrication of diamond surface and bulk structures”

S. Sciortino, M. Bellini, F. Bosia, S. Calusi, C. Corsi, C. Czelusniak, N. Gelli, L. Giuntini, F. Gorelli, S. Lagomarsino, P. A. Mandò, M. Massi, P. Olivero, G. Parrini, M. Santoro, A. Sordini, A. Sytchkova, F. Taccetti, M. Vannoni

*Nuclear Instruments and Methods in Physics Research B 348, 191-198
(2015)*

DOI: 10.1016/j.nimb.2014.11.061

The definitive version is available at:

La versione definitiva è disponibile alla URL:

<http://www.sciencedirect.com/science/article/pii/S0168583X14009422>

MICRO-BEAM AND PULSED LASER BEAM TECHNIQUES FOR THE MICRO-FABRICATION OF DIAMOND SURFACE AND BULK STRUCTURES

S. Sciortino^{1,2}, M. Bellini^{3,4}, F. Bosia^{5,6}, S. Calusi^{1,2}, C. Corsi^{1,3}, C. Czelusniak^{1,2}, N. Gelli², L. Giuntini^{1,2},
F. Gorelli^{3,4}, S. Lagomarsino^{1,2}, P. A. Mandò^{1,2}, P. Olivero^{5,6,7}, G. Parrini¹, M. Santoro^{3,4}, A. Sordini⁴,
A. Sytchkova⁸, F. Taccetti², M. Vannoni^{4,*}

¹*Dipartimento di Fisica e Astronomia, Università di Firenze, Via Sansone 1, I-50019, Sesto Fiorentino, Firenze, Italy*

²*Istituto Nazionale di Fisica Nucleare (INFN), Sezione di Firenze, Via Sansone 1, I-50019, Sesto Fiorentino, Firenze, Italy*

³*European Laboratory for Non-Linear Spectroscopy, Via Nello Carrara 1, 50019 Sesto Fiorentino (FI), Italy*

⁴*Istituto Nazionale di Ottica (INO-CNR), Largo Enrico Fermi 6, 50125 Firenze (FI), Italy*

⁵*Physics Department and “Nanostructured Interfaces and Surfaces” inter-departmental centre, University of Torino, via P. Giuria 1, 10125 Torino, Italy*

⁶*INFN Sezione di Torino, via P. Giuria 1, 10125 Torino, Italy*

⁷*Consorzio Nazionale Interuniversitario per le Scienze Fisiche della Materia (CNISM), via della Vasca Navale 84, 00146 Roma, Italy*

⁸*ENEA Optical Coatings Group, via Anguillarese 301, 00123 Rome, Italy*

**Present address: European XFEL GmbH, Notkestraße 85, 22607 Hamburg, Germany.*

Abstract

Micro-fabrication in diamond is applicable in a wide set of emerging technologies, exploiting the exceptional characteristics of diamond for application in bio-physics, photonics, radiation detection. Micro ion-beam irradiation and pulsed laser irradiation are complementary techniques, which permit the implementation of complex geometries, by modification and functionalization of surface and/or bulk material, modifying the optical, electrical and mechanical characteristics of the material. In this article we summarize the work done in Florence (Italy), concerning ion beam and pulsed laser beam micro-fabrication in diamond.

Introduction

Micro-beam ion implantation in the MeV range and laser micro-fabrication are techniques exhibiting largely complementary features. The relatively short range of MeV implantation makes it useful for the fabrication of structures parallel to the surface of the sample at depths ranging from a few to tens of micrometers, with a vertical resolution limited by the width of the Bragg peak and a lateral one better than one micrometer, in the most recent high performance setups [1]. The types of structural modification allowable by ion implantation range from electrical [2] to optical [3-5], mechanical and chemical [6]. Laser material engineering, on the other hand, depending on wavelength, energy and pulse width, is useful in ablation or amorphization of the material [7,8], and is suitable for the modification of the surface or of the interior of the sample (up to centimeters, theoretically), with a lateral resolution comparable to that of the micro-beams but with a vertical definition (in the bulk) limited by the focusing aperture to about ten micrometers.

In diamond, these two techniques could pave the way to the integration of micro-devices with applications in particle detection, bio-sensing, micro-optics and quantum-optics. Both ion damaging (followed by appropriate annealing [9,10]) and sub-bandgap pulsed laser irradiation are capable of increasing the conductivity of the material by modification of the bonding hybridization, from sp^3 to sp^2

1
2
3 [11]. Thus, micro-beam writing can be employed in the fabrication of conductive channels or pads
4 under the surface of diamond, while pulsed laser graphitization is suitable for fabrication of conductive
5 columns, perpendicular to the surface, or of conductive channels, at the surface level. In this way,
6 electrodes inside diamond can be implemented in three-dimensional diamond detectors, or in micro-
7 electrodes arrays employed in studies on biological tissues [12,13], or in Stark-effect tuned optical
8 micro-cavities [14], just to mention some of the possible applications. Moreover, the optical
9 modification of the material induced by ion implantation can be used to implement light guides in
10 micro-optical devices. Doping by ion implanting can be employed both in tailoring the band-gap of
11 diamond and in deterministic implantation of color centers for quantum applications. On the other
12 hand, laser ablation[15] and micro-beam graphitization, followed by chemical etching [16], are useful
13 to model the surface of the material for applications ranging from biophysics to optics.

14 For all these applications, ion beams of different species and at different current levels are needed
15 together with different types of pulsed laser beams. At the LABEC laboratories of Florence, Italy, we
16 can employ two lines of a 3 MV tandem accelerator: the external micro-beam setup with a lateral
17 resolution of 10-20 μm for modification of the optical and electrical properties of the material [17], and
18 and an electrostatically deflected beam for very low-current level implantations [18]. At the LENS
19 laboratories, also in Florence, a pulsed laser apparatus is arranged with two different laser lines on a
20 same optical setup: a 30 fs, 800 nm Ti-sapphire laser and an 8 ns, 1064 nm Nd:YAG laser source, both
21 operating in the micro-joules per pulse range [11]. Several techniques are employed to characterize the
22 artifacts: electrical characterization at the laboratories of INFN (Florence), geometrical profiles and
23 refractive index measurements at the at the INO laboratories (Florence), Raman characterization at the
24 LENS laboratories.

25 In this article, we review the work done in Florence in the micro-modification of the structural
26 properties of diamond (in collaboration with the Departments of Physics and INFN of Turin and the
27 CNR of Rome). Work has been done in micro-beam modification of the optical properties of diamond
28 [19-23], micro-beam writing of optical waveguides in the bulk diamond [21,24], pulsed laser
29 fabrication of buried and superficial conductive channels [11,12], fabrication of three-dimensional
30 diamond particles detectors [25]. All the expertise acquired in the fabrication and characterization of
31 micro-structures in diamond can be considered ready to use for the realization of diamond integrated
32 devices.

33 **1. Modification of the complex refractive index due to ion implantation**

34 In this section we report on the refractive index modification of high quality, Chemical Vapour
35 Deposited (CVD) IIa diamond samples, irradiated with 2 and 3 MeV protons.

36 **Ion implantation**

37 The diamond samples were implanted at the external scanning micro-beam facility [26] of the 3 MV
38 Tandatron accelerator of the INFN LABEC Laboratory in Florence. The sample to be implanted was
39 kept out of vacuum, thus allowing its easy handling, positioning and monitoring [27].

40 Proton beams were focused on the polished side of the samples to a spot (FWHM) of around 10 μm (3
41 MeV) or 20 μm (2 MeV). Different zones of the samples were implanted at fluences ranging from
42 $10^{15} / \text{cm}^2$ to $10^{17} / \text{cm}^2$.

43 The overall precision on the implanted charge determination is about 1%. Possible systematic errors in
44 the charge determination, affecting all the experimental points with a common scale factor, amount to
45 10% of the measured value. After ion implantation, the size of the irradiated area was measured on the
46 optical path difference maps as described below, the resulting precision on the area determination is
47 about 2%.

Measurement of the optical path difference and the absorption length difference

In order to evaluate the optical path difference due to ion-induced damage, the phase shift of a laser beam crossing the damaged diamond layer was determined, using a commercial laser interferometric microscope (Maxim 3D, Zygo Corporation, USA) with a $20 \times$ micro-Fizeau objective, operating with the $\lambda_{\text{He-Ne}} = 632.8$ He-Ne laser line. The horizontal and vertical resolutions were, respectively, $1.68 \mu\text{m}$ and 0.63 nm , and the field view of $349 \times 317 \mu\text{m}$ [19]. In this instrument, a He-Ne laser beam is properly expanded to invest the full area of the sample; the micro-Fizeau objective contains a beam-splitter that reflects part of the light (“reference beam”), while the remaining part crosses the sample and is reflected from a high-quality external mirror (“test beam”). The diamond is slightly tilted to avoid undesired internal reflections between the two opposite surfaces of the sample. The interference pattern of the reference and test beam is recorded by a CCD camera.

Using the phase shift method [28] it is possible to reconstruct the relative phase Δ of the test beam at each pixel: the contributions of the beam splitter and the high-quality mirror is accounted for and removed. The phase difference Δ reflects the optical path difference:
$$\Delta = \frac{2\pi}{\lambda_{\text{He-Ne}}} OPD$$

The absorption length difference was evaluated, for each implantation, by the ratio between the transmittance T_0 of the unimplanted substrate and the value T measured through a chosen damaged area:

$$ALD = \frac{\lambda}{4\pi} \log\left(\frac{T_0}{T}\right)$$

The transmittance spectra were acquired with a setup described in Ref. [20].

Both the optical path difference and the absorption length difference measurements are affected by swelling, i.e., the expansion of the implanted material, which determines both a further phase shift of the probe laser beam and an additional absorption contribution. Nevertheless, since the gradient of the displacement of each layer in diamond $\frac{dz'}{dz}$ and the relative variation of the refractive index $\frac{\Delta n}{n}$

are both small with respect to unity, it can be shown [21] that the values of OPD and ALD due to the variation of the refractive index alone can be obtained by the measured ones (OPD_m, ALD_m), by the simple equations:

$$OPD = OPD_m - (n_0 - 1)h$$

$$ALD = ALD_m - \kappa_0 h$$

where h is the swelling height, n_0 and κ_0 , respectively, are the index of refraction and extinction coefficients of undamaged diamond. The parameter h has been measured by means of a white-light interferometry microscope (Newview, Zygo Corporation).

In our measurements, the product $k_0 h$ is negligibly small (well below 0.1%) and its contribution has been neglected, but the product $(n_0 - 1)h$ amounts to about 15% of the measured optical path difference, and it has been properly subtracted.

Results and Discussion

A linear model has been exploited [22] to interpret the optical path difference and absorption length difference measurements in terms of the modification of the real and of the imaginary part of the refractive index, taking into account the damage profile produce by 2 and 3 MeV protons and calculated by means of a Monte Carlo SRIM simulation. The optical path difference and the absorption length difference are linear in the ion fluence and are proportional to the average number I^E of vacancies produced by each ion of specific energy E . Figure 1 shows how the ratio OPD/I^E is proportional to the fluence and independent on the energy; for the absorption length difference a similar

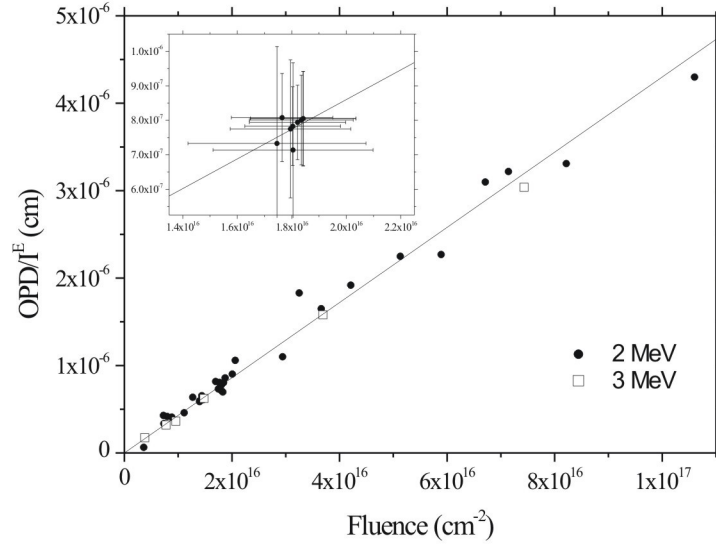


Figure 1. Linear trend of the $OPD(E, \phi)/I(E)$ ratio as a function of the fluence ϕ . In the inset: particular of the points representing eight different implantations at a same nominal fluence but with different values of the instantaneous current (a factor 5 of variation).

plot has been obtained [22].

It results that the ion induced complex refractive index, for fluences up to the highest reached in our experiments, can be expressed as:

$$\bar{n} = 2.41 + [(4.84 \pm 0.05) + i(2.86 \pm 0.04)] \times 10^{-23} \text{ cm}^3 \rho \quad (1)$$

where ρ is the vacancy density produced by the irradiation in vacancy/cm³. The experimental results point out that the variation of the refractive index depends only on the overall vacancy density induced by the radiation during the process, irrespectively of the ion energy and of the beam intensity.

Previous works about the optical characteristics of ion-damaged diamond [29-32] also report increasing trends of the real part of the refractive index. The linear coefficients, although determined with much higher uncertainty, are compatible with the results summarized by Eq. 1. In a very early report [29], the refractive index of diamond implanted with 20 keV C⁺ ions exhibits a monotonic increase as a function of implantation fluence, with linear coefficients strongly dependent on the measured sample and ranging from about 2 to 10 × 10⁻²³ cm³.

The linear dependence holds up to a damage level at which the refractive index seems to saturate; such saturation level corresponds to a total atomic concentration of 4.5 × 10²¹ vacancy cm⁻³, a value slightly exceeding the maximum damage density explored in the present work (2.5 × 10²¹ vacancies cm⁻³). For one of the four diamond samples reported in ref. [29] (sample I), the dependence of the refractive index from the damage density is in very satisfactory agreement with our result, while other samples exhibit rather different trends. From such a very early report it is not possible to reconstruct the types of the different diamond samples employed.

Differently from what reported in [33], in [30] no clear trend emerges in the variation of the refractive index and therefore a direct comparison with the present work is difficult. In [32] the authors report a low value of the refractive index for the heavily damaged buried layers, whose damage-induced

1
2
3 vacancy density amount to about $4 \times 10^{22} \text{ cm}^{-3}$. Under these conditions, the degree of
4 amorphization/graphitization exceeds by far what reported in the present work. Finally, it is worth
5 remarking that the results of this work are in good agreement with recent ellipsometric studies of the
6 refractive index variation in shallow layers implanted with 180 keV B ions, for which consistent
7 linearly increasing trends are reported in the at low damage density regime [30]. In particular, at
8 wavelength 632.8 nm, a linear coefficient of $(3.8 \pm 0.3) \times 10^{-23} \text{ cm}^{-3}$ can be obtained for the dependence
9 of the real part of the refractive index, in satisfactory agreement with the value reported in this work,
10 particularly if it is considered that different implantation conditions and analytical techniques were
11 employed.
12

13
14 The increasing trend of the refractive index as a function of induced damage is somewhat surprising
15 with respect to what reported in other materials, such as quartz [33] or zircon [34], for example. This is
16 because the most direct effect of ion implantation in crystals usually consists in the progressive
17 amorphization of the substrate, which invariably leads to a decrease of the atomic density and therefore
18 of the refractive index. Although often quantitatively predominant, the above-mentioned process is not
19 the only effect determining a variation in refractive index. Beside volume expansion, other damage-
20 related effects can occur which have a significant and direct effect on the refractive index, namely
21 changes in atomic bond polarizability and structure factors, as expressed by the Wei adaptation of the
22 Lorentz-Lorenz equation [35]:
23
24

$$\frac{\Delta n}{n} = \frac{(n^2 - 1)(n^2 - 2)}{6n^2} \left(-\frac{\Delta V}{V} + \frac{\Delta \alpha}{\alpha} + F \right)$$

25
26
27
28
29
30 where V is the volume, α is the polarizability and F is the structure factor of the target implanted
31 material.
32

33 Although the volume expansion term is dominating in most cases, the structural modification results in
34 changes of the chemical bonds and subsequently of the material polarizability. Such changes can be
35 either positive or negative in sign and, therefore, it is reasonable to expect strong polarizability-related
36 effects in a peculiar material such as diamond, in which the nature of the chemical bond can be
37 subjected to drastic changes (i.e. from the strongly covalent sp^3 bonds to sp^2 bonds).
38

39 While for low damage levels (well below the amorphization threshold, as mentioned above),
40 polarizability-related effects related to the formation of isolated sp^2 defects can dominate over the
41 volume effects, it is reasonable to expect that at higher damage levels the amorphization of the diamond
42 sp^3 lattice can lead to predominant density effects and thus to the reduction of the refractive index, as
43 indeed observed in [32].
44

45 Concerning the increase of the imaginary part of the refractive index, we note that this can be related to
46 defect-induced optical transitions and, to a lesser extent, in absorption due to conductivity. A model of
47 hopping conduction between graphitic defect centers formed in the ion tracks has been proposed [36].
48 According to this model, at a critical dose the connectivity between centres causes percolation and a
49 sharp decrease in resistivity, which is not likely to occur in our case, since we are below the
50 graphitization threshold, i.e., we verified a recover of the diamond phase after dose implantation and
51 thermal annealing at 1100 C.
52
53

54 We conclude by remarking that further investigation should be necessary to ascertain if the same
55 mechanisms occur also for the damage induced by other ion species, but the present work indicates that
56 a proton beam can be used in tailoring the optical properties of diamond in the MeV range with the
57 help of a common damage simulation software such as SRIM. The methodology of measurements and
58 analysis which adopted for this study is of ease and versatile use, for application for any transparent
59 material within very large range of energies and fluences.
60
61
62
63
64
65

2. Waveguides engineering in single crystal diamond by MeV proton implantation

Ion implantation of the waveguides

To perform this study, three surfaces of a Ila monocrystalline CVD diamond were optically polished to a roughness of 1 nm: the two opposite $3.0 \times 3.0 \text{ mm}^2$ faces and one of the four lateral $3.0 \times 0.5 \text{ mm}^2$ faces down to a roughness of some nanometers. To obtain controlled increments of the refractive index a 3 MeV proton beam was focused on the small polished side of the sample to an approximately Gaussian spot, $12 \mu\text{m}$ wide, and scanned along a $500 \mu\text{m}$ rectilinear path perpendicular to the large polished faces (longitudinal direction of the guide, see the schematics of Fig. 2 [24]). The fluences were 2×10^{16} , 1×10^{16} , $5 \times 10^{15} \text{ cm}^{-2}$ in the central region of each implantation, with an estimated uncertainty not exceeding 5%. The resulting vacancy density distribution, as calculated using SRIM Monte Carlo simulations, follows the characteristic distribution, also recalled in Fig. 2 (left panel), peaked at a depth of approximately $50 \mu\text{m}$.

Optical characterization and interpretation of data

The as-prepared structures were then observed with the Maxim interferometer, previously used to characterize refractive index variations by measuring the optical path difference. In this case the phase maps obtained with the micro-interferometer can be interpreted as a direct measurement of the amplitudes of the modes propagating along the guide.

As the structures under consideration have a cross-sectional dimension comparable to that of the wavelength of the radiation, the radiation emerging from the diamond will be given by a principal plane-wave part plus a perturbation produced by the structures themselves. Consequently, the field will be given by the sum of three contributions.

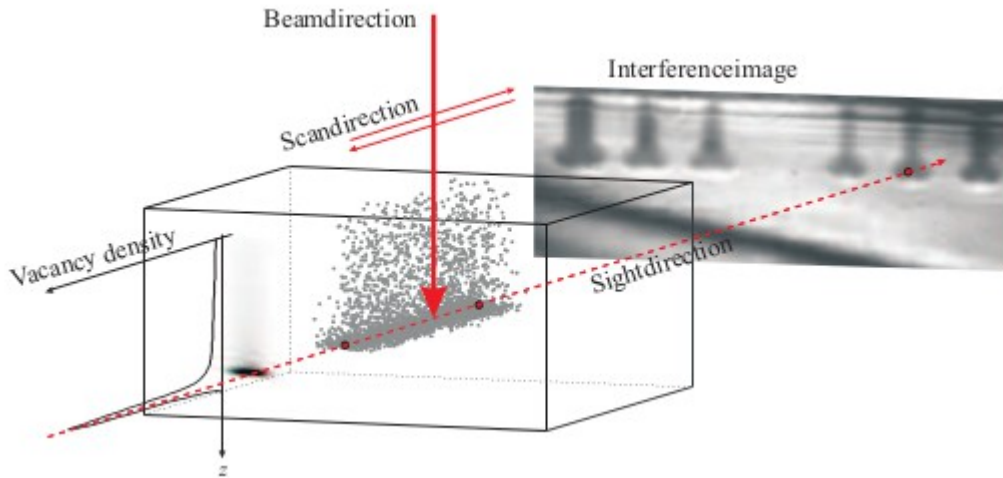


Figure 2. Schematics of the implantation geometry and the resulting interference pattern. Implantation fluences from left to right: $2 \times 10^{16} \text{ cm}^{-2}$ (one implantation), $1 \times 10^{16} \text{ cm}^{-2}$ (two implantations), $5 \times 10^{15} \text{ cm}^{-2}$ (the last three implantations).

These are: a principal part given by the radiation reflected back by the interferometer mirror

$$E_0 = \mathcal{E}_0 e^{i[\omega t + \varphi_0]}$$

a secondary field deriving from the reflections on the surfaces of the sample

$$E_R = \mathcal{E}_R(x, y) e^{i[\omega t + \varphi_R(x, y)]}$$

1
2
3 and a perturbation given by the contribution to the field of the structures under consideration. If the
4 field can be considered as guided by the structures, this contribution can be simply written as

$$5 \quad E_G = f(x, y) e^{i(\omega t + \varphi_G)}$$

7 where the function $f(x, y)$ is the amplitude map of the mode or a sum of different amplitudes maps.

8 If \mathcal{E}_R and f are both small compared with \mathcal{E}_0 , the phase difference $\Delta\varphi = \varphi(x, y) - \varphi_0$, measured
9 by the instrument, is given, at the lowest order, by:

$$10 \quad \Delta\varphi(x, y) = \frac{\mathcal{E}_R(x, y)}{\mathcal{E}_0} \sin(\varphi_R(x, y) - \varphi_0) + \frac{f(x, y)}{\mathcal{E}_0} \sin(\varphi_G - \varphi_0)$$

13 Consequently, once the contribution of the reflections has been fitted and subtracted, the map of $\Delta\varphi$ is
14 simply proportional to the amplitude map of one of the modes which can propagate in the structure, or
15 to a linear combination of several modes simultaneously propagating in the waveguide, each with its
16 appropriate phase value φ_G .

17 For the calculation of the field modes, a 2-dimensional finite element model (FEM) of the irradiated
18 regions was employed, taking into account the local modifications in the refractive index induced by
19 proton damage, quantified in terms of the induced vacancy density and calculated by means of a Monte
20 Carlo simulation (SRIM). Once given the vacancy density at every cell of the simulation grid, the local
21 variation of refractive index at the He-Ne wavelength of 632.8 nm is calculated from the simple
22 relation (1). Then, the experimentally obtained phase maps were compared with a superposition of the
23 calculated amplitude maps, by fitting them with a linear combination of the propagating modes. Since
24 the relative amplitudes of the modes excited in the waveguides depend in a sensitive way from the
25 illumination conditions, different positions of the sample on the focal plane may imply different
26 weights to be assigned at each particular mode. In Figure 3 different images of the implantations at
27 fluencies of 2×10^{16} , 1×10^{16} and $0.5 \times 10^{16} \text{ cm}^{-2}$ are shown along with the best fit obtained with 30
28 different propagation modes (ten for each structure) and two plane sinusoids, taking into account the
29 reflections on the two planes. It is evident that the same set of propagation modes, although with
30 different weights, fits the different images. From the inspection of these images we conclude that the
31 adherence of the fit to the experimental two-dimensional profiles is very good in the cap layer between
32 0 and about 45 μm in depth, where the relative damage is small, while at end-of-range the structures
33 seem to be more diffuse, probably due to the distortion induced by diffraction on the highly opaque
34 regions, in correspondence with the considered structures.

41 **3 Laser graphitization of diamond**

42
43 In this section we describe surface and bulk laser graphitization of diamond aimed to fabricate (three-
44 dimensional) diamond-based radiation detectors. The experimental setup described in [11] employs two
45 pulsed laser sources:

46 a) a Nd:YAG Q-switched source with an 8 ns pulse width, 1064 nm wavelength, pulse energies in the
47 range 10–60 μJ and repetition rates from 1 to 10 kHz.

48 b) a Ti-sapphire femtosecond laser source of 30 fs pulse width, 800 nm wavelength, pulse energy
49 between 3 and 18 μJ and repetition rate of 1 kHz.

50 Both beams have been focused either on the diamond surface or in the diamond bulk. The samples used
51 were Element Six high-purity monocrystalline $4.5 \times 4.5 \times 0.5 \text{ mm}^3$ and polycrystalline $5 \times 5 \times 0.5$
52 mm^3 CVD diamond plates.

53 The graphitic structures we implemented are:

54 A) superficial conductive tracks obtained by keeping the front surface of the diamond in the focal plane
55 of the objective and translating it at constant velocity (xy- directions);

56 B) buried conductive wires obtained by focusing the laser beam on the back diamond surface and
57 moving the focus at constant velocity perpendicularly to the surface, across the bulk for 100– 500 μm

(z-direction).

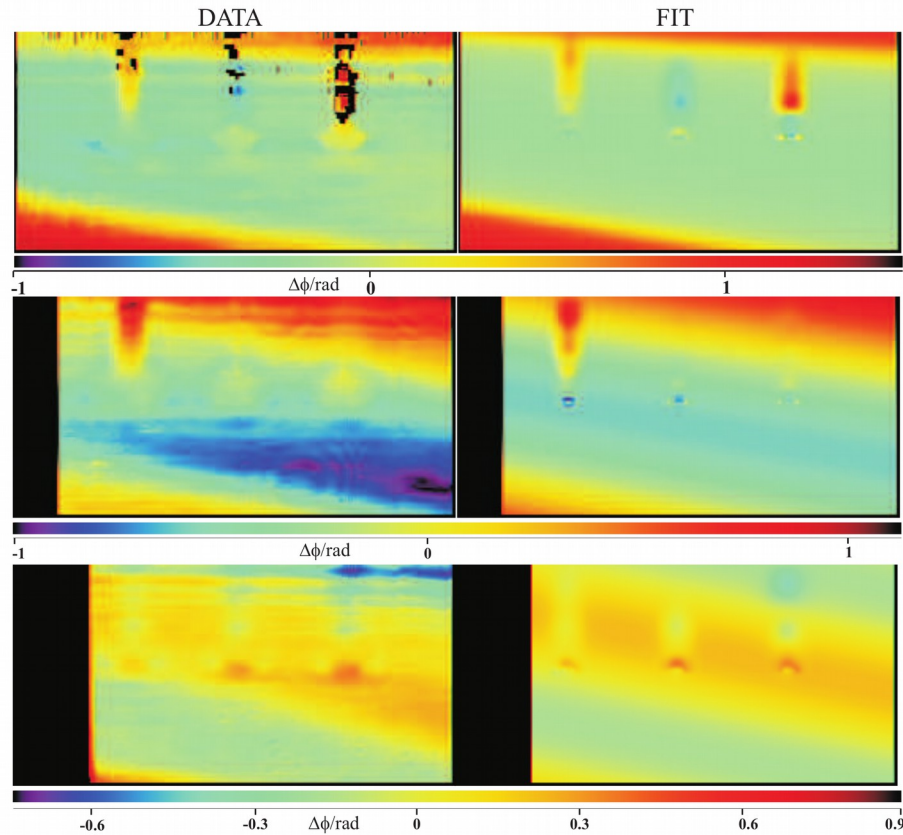


Figure 3. Comparison of the measured phase shift maps (left) and of the fit (right) obtained by linear superposition of modes amplitudes and a background taking into account multiple reflections effects. Top and middle: images obtained from three adjacent guides irradiated at $2 \times 10^{16} \text{ cm}^{-2}$ (the left one) and at $1 \times 10^{16} \text{ cm}^{-2}$ (the others). Bottom: images obtained by three equally irradiated guides at a fluence of $5 \times 10^{15} \text{ cm}^{-2}$.

Structural and electrical characterization

Only the ns-pulsed laser source appears to be useful in fabrication of superficial conductive tracks, because the fs-laser source causes ablation of diamond, and leaves only a very thin layer of modified material. The ns-laser source causes a relatively low ablation creating deep (up to $50 \mu\text{m}$) and narrow ($\approx 10 \mu\text{m}$) grooves uniformly filled with an opaque material. The depth of the grooves increases with the number of laser pulses (up to about $50 \mu\text{m}$ at about 700 pulses/point). On the contrary it is quite independent of the pulse energy (at least up to $50 \mu\text{J/pulse}$), provided that the energy lies above a threshold of about $6 \mu\text{J/pulse}$. This is the threshold found if the irradiation starts from a zone where the material is already graphitized, while if the graphitization has to start from undamaged diamond the threshold is placed at about $37 \mu\text{J/pulse}$.

The resistivity of the modified material, as measured on different tracks, fabricated with different energy per pulse and number of pulses per point, is $8 \pm 4 \text{ m}\Omega \text{ cm}$, which is not so far from those reported for amorphous graphite, with no clear dependence on the process parameters.

Raman characterization confirms that the modified material consists in a phase of disordered sp^2 carbon [11]. we found invariantly a feature with two wide peaks: one centered at 1580 cm^{-1} (G peak of

1
2
3 graphite) and one whose position depended on the excitation wavelength, identified as the D peak of
4 disordered graphite [37].

5 Both the sources we employed are capable to write buried conductive channels perpendicular to the
6 beam entrance surface of diamond, but with different geometrical and physical characteristics. The
7 cross-sectional area of both types of structure depends on the pulse energy, being roughly proportional
8 to the difference between the pulse energy and a threshold value which is about 2 μJ for the fs-pulsed
9 laser source and 9 μJ for the ns one, over an irradiated area of about 50 μm^2 (corresponding to an
10 energy density of the order of 10 J/cm^2). In the case of ns-pulsed laser, in order to grow a buried
11 column with such a low value of the energy per pulse, it is necessary to initiate it on an already
12 graphitized zone on the back side of the diamond sample. The morphological characteristics of the two
13 kinds of columns are quite different: ns-laser made structures are quite irregular in cross-section and
14 exhibit cracks which are more and more evident as the value of the energy per pulse increase. On the
15 contrary, fs-laser made columns are more regular in section and show traces of ruptures only for very
16 high values of the energy per pulse employed. The two types of wires also exhibit a very different
17 electrical behavior. The mean resistivity obtained for the ns-source wires was about 60 $\text{m}\Omega\text{cm}$, while
18 that for the fs-source wires was an order of magnitude greater (about 900 $\text{m}\Omega\text{cm}$) in agreement with
19 Kononenko et al. [38]. The Raman spectra of the buried structures were observed through the lateral
20 polished surface of the diamond plate. The columns were grown inside the diamond bulk at distance of
21 about of 40 μm from that surface that acted as an optical window.

22 The Raman analysis of the two kinds of structures explains the difference in their electrical behavior.
23 The 1332 cm^{-1} (165 meV) line of diamond is superimposed to the D peak, due to the 40 μm -thick layer
24 of diamond in front of each column, and a distinct G peak at 1580 cm^{-1} (196 meV) is clearly
25 observable. Moreover, a feature at 1090 cm^{-1} (135 meV) is seen, in the structures fabricated with the
26 ns-pulsed laser source, around the graphitic structures within a distance of a few micrometers. This
27 peak is attributed to nano-crystalline diamond [39], or to Z-carbon [40], an sp^3 phase which is stable at
28 pressures exceeding about 9.8 GPa. The local pressure has been determined from the stress-induced
29 deformation of the diamond line at 1332 cm^{-1} .

30 A quantitative analysis was carried out taking as an index r of the graphitic content of the graphitic
31 structures the ratio between the G-peak area and the area of the 1332 cm^{-1} peak of unmodified diamond
32 at the same depth. Bidimensional maps of the graphite contents in the modified regions were derived
33 from this analysis [11]. It can be observed that the maximum r index measured in the structures created
34 with the nanosecond laser source is one order of magnitude larger than that of the femtosecond
35 structures. Therefore the resistivity values of differently fabricated structures are related to the different
36 content in graphite of the material. In both cases we interpret these results in terms of a mixture of two
37 phases in which conduction takes place by percolation between graphite micro or nano-crystals
38 dispersed in an sp^3 matrix.

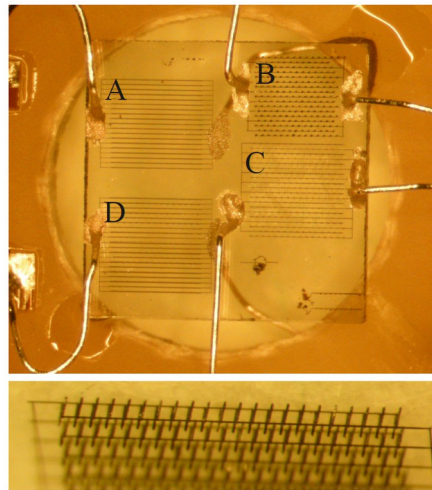
39 Bidimensional maps of the pressure gradient in the modified region of the graphitic channels was
40 derived from the analysis of distortion/shift of the diamond Raman line [41].

41 From the maps it becomes apparent that the regions occupied by the graphitic phase and by the sp^3
42 nanostructured phase are related to a compressive stress in the diamond around them which can be as
43 high as 10 GPa, not so far from the maximum pressure for which graphite is stable at the thermo-
44 dynamic equilibrium, that is the graphite–diamond–liquid triple point pressure, at about 13 GPa [42].
45 This explains the reduced graphitic content and the high values of resistivity of the buried material. The
46 very high elastic constants of diamond and graphite and the low density of graphite with respect to
47 diamond would determine, in the case of a complete transformation of diamond in graphite, very high
48 pressure of the buried graphitic phases, which can be estimated in about 60 GPa. But graphite is stable
49 at the thermodynamic equilibrium only below about 13 GPa. Consequently, only a high density mixed
50 phase can crystallize, in a way that the local pressure never exceeds, after the phase formation, those
51 permitted by thermodynamics. A high density phase can be obtained only in a material relatively poor
52
53
54
55
56
57
58
59
60
61
62
63
64
65

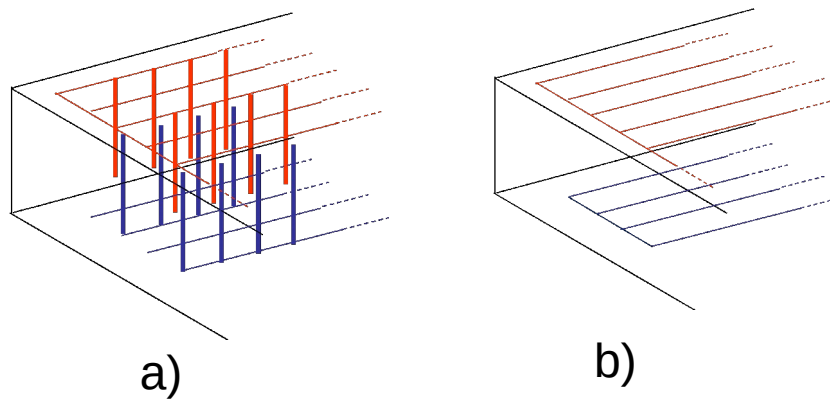
1
2
3 of sp^2 bonds, determining an intrinsic higher resistivity of the buried graphitic electrodes with respect
4 to the surface ones.

5 We also observe that a conductivity model involving percolation between damaged regions also been
6 proposed in the case of ion implantation over a critical dose [43], giving a very similar picture to the
7 one we propose.
8

9 An investigation is under way to model the processes of excitation and relaxation occurring during the
10 laser irradiation from low field to the graphitization threshold. Experimental data and simulations agree
11 on the fact that the excitation in the femtosecond regime is a non linear process involving four photons
12 and five photons ionizations [44]. An evaluation of the lattice temperature, after a further refinement of
13 the model, is likely to show the non-thermal nature of the graphitization process. The situation in the
14 nanosecond regime is obviously quite different but at present poorly understood. Experimentally a
15 higher threshold is needed and the result is highly unpredictable particularly in the diamond bulk,
16 suggesting that the process is much more ruled by the presence of defects acting as seeds for the
17 graphitization to occur.
18
19
20



21
22
23
24
25
26
27
28
29
30
31
32
33
34
35
36
37
38
39 Figure 4. Top. four different sensors fabricated on a single crystal diamond A:Reference planar
40 sensor; B: fs-made sensor; C-D ns-made sensors; D: OSC ns-made sensor. Bottom. Detail of a 3D
41 fs-made sensor.
42
43



44
45
46
47
48
49
50
51
52
53
54
55
56
57
58
59 Figure 5. Schematics of (a) the reference sensor and (b) the "opposite comb" 3D sensor (see text.)
60
61
62
63
64
65

Three-dimensional diamond detectors

The concept of three-dimensional detectors has been conceived for silicon detectors [44] in order to improve the radiation resistance of solid state detectors. In the last years the concept has been also applied to diamond [25, 46, 47], exploiting the pulsed laser writing techniques made available in the meantime, mainly for optical applications [8].

We fabricated different sensors made on monocrystalline and polycrystalline high purity CVD 0.5 mm thick diamond. Fig. 4 shows an image of four different sensors fabricated on a single crystal diamond.

Figure 5 (a) show the schematics of a 3D detector “with opposite side combs” where the columns of each array begin at one surface and end at a distance of about 80 μm from the opposite one, so that no superficial conduction could occur between neighbours. Two different superficial conductive combs are made at the two opposite surfaces of the sample to connect the columns of each array at the bias. The processing time of each column is about 10 s, in a way that the fabrication of a 3D sensor requires from 20 to 40 minutes per mm^2 , according to the inter-electrode distance.

The structure is formed by the repetition of “elementary cells” in which two oppositely polarized columns lie, respectively, at a vertex and at the center of the cell. The dimensions of the elementary cell was from $70 \times 114 \mu\text{m}^2$ to $100 \times 160 \mu\text{m}^2$. The diameter of each column is about 10 μm and 5 μm for the fs-laser-made columns and for the ns-ones, respectively. Reference structures (Fig. 5 (b)) were also fabricated, implementing with the ns laser two graphitic combs, with a pitch of 80 μm , on the two sides of the samples, without buried columns, in order to compare the performances of the 3D structures with a conventional planar sensor. The collection efficiency of the sensors to relativistic beta particles has been measured using a setup described in detail in ref. [48]. In Figure 6 the dependence of the average signal on the bias voltage is shown for the reference and for the 3D fs-made sensor in the monocrystalline sample. The figure also shows the statistical distribution of the signals for the two sensors at saturation. Full collection (19000 electrons) occurs for both sensors, confirming that superficial graphitic electrodes fabricated with the nanosecond laser source do not exhibit signal loss (see also Ref. [12]) and demonstrating as well that the femtosecond buried columns are suitable electrodes for charge collection. Moreover signal saturation for the 3D sensor (which depends on the applied electric field) occurs at a bias voltage one order of magnitude lower than that of the reference sensor. This confirms that charge transport takes place between electrodes whose interdistance is much lower than the sensor thickness.

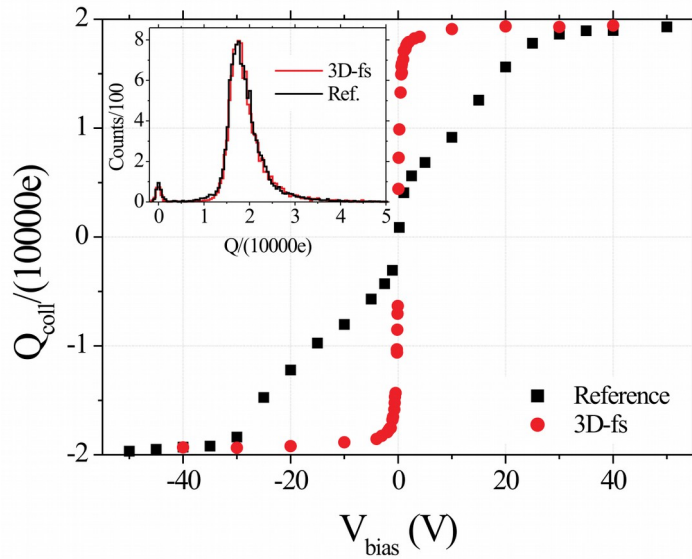


FIG. 6. Mean signal of two sensors fabricated on the same monocrystalline diamond, a reference conventional planar detector and a 3D-fs sensor in the IDC configuration. In the inset, the signal distribution from the two sensors at saturation voltage

An emerging feature, in all the sensors fabricated to date, is the lower response of the 3D-devices fabricated with the nanosecond laser, compared with the reference or with the corresponding fs-made structures fabricated in the same kind of diamond, justified in terms of the nanocrystalline sp^3 defective phase evidenced by Raman characterization [25]. The fs-columns are undoubtedly more efficient, but their electrical resistance is higher resulting in a higher Johnson noise in implemented 3D detector devices, which can be a substantial drawback. A better tuning of the graphitization parameters is required to minimize this defective layer.

Conclusion

All the expertise acquired in the fabrication and characterization of micro-structures in diamond can be considered ready to use for the realization of diamond integrated devices. Particularly, work is in progress to integrate horizontal and vertical graphitized structures fabricated with different techniques.

References

- [1] F. Watt, A.A. Bettiol, J.A. Van Kan, E.J. Teo, M.B.H. Breese, Ion beam lithography and nanofabrication: a review, *Int. J. Nanosci.* 04, 269 (2005). DOI: 10.1142/S0219581X05003139
- [2] P. Olivero, G. Amato, F. Bellotti, O. Budnyk, E. Colombo, M. Jakšić, C. Manfredotti, Ž. Pastuović, F. Picollo, N. Skukan, M. Vannoni, E. Vittone. Direct fabrication of three-dimensional buried conductive channels in single crystal diamond with ion micro-beam induced graphitization. *Diamond & Related Materials* 18 (2009) 870–876

- 1
2
3 [3] A. Benayas, D. Jaque, Y. Yao, F. Chen, A. A. Bettiol, A. Rodenas, and A. K. Kar. “Microstructuring
4 of Nd:YAG crystals by proton-beam writing”. *Opt. Lett.* 35 (2010) 3898–3900
5
6
7
8
9 [4] M. A. Draganski, E. Finkman, B. C. Gibson, B. A. Fairchild, K. Ganesan, N. Nabatova-Gabain, S.
10 Tomljenovic-Hanic, A. D. Greentree, and S. Prawer. “Tailoring the optical constants of diamond by ion
11 implantation”. *Optical Materials Express* 2 (2012) 644-649
12
13
14
15
16 [5] A. A. Bettiol, S. V. Rao, E. J. Teo, J. A. van Kan, and F. Watt, “Fabrication of buried channel
17 waveguides in photosensitive glass using proton beam writing,” *Appl. Phys. Lett.* 88(17), 171106
18 (2006).
19
20
21
22
23 [6] B. A. Fairchild, P. Olivero, S. Rubanov, A. D. Greentree, F. Waldermann, R. A. Taylor, I.
24 Walmsley, J. M. Smith, S. Huntington, B. C. Gibson, D. N. Jamieson, and S. Prawer, “Fabrication of
25 Ultrathin Single-Crystal Diamond Membranes,” *Adv. Mater. (Deerfield Beach Fla.)* 20(24), 4793–4798
26 (2008).
27
28
29
30
31 [7] T.V. Kononenko, V.G. Ralchenko, I.I. Vlasov, S.V. Garnov, V.I. Konov. “Ablation of CVD diamond
32 with nanosecond laser pulses of UV–IR range”. *Diamond and Related Materials* 7 (1998) 1623–1627
33
34 [8] T.V. Kononenko, M.S. Komlenok, V.P. Pashinin, S.M. Pimenov, V.I. Konov, M. Neff, V.
35 Romano, W. Lüthy, “Femtosecond laser microstructuring in the bulk of diamond”. *Diamond Relat.*
36 *Mater.* 18 (2009) 196–199.
37
38
39 [9] C. Uzan-Saguy, C. Cytermann, R. Brener, V. Richter, M. Shaanan, and R. Kalish. “Damage
40 threshold for ion-beam induced graphitization of diamond”. *Appl. Phys. Lett.* 67 (1995), 28
41
42
43 [10] P. F. Lai, S. Prawer, L.A. Bursill. “Recovery of diamond after irradiation at high energy and
44 Annealing”. *Diamond and Related Materials* 10 (2001) 82-86
45
46
47 [11] S Lagomarsino, M Bellini, C Corsi, S Fanetti, F Gorelli, I Lontos, G Parrini, M Santoro, S
48 Sciortino, Electrical and Raman-imaging characterization of laser-made electrodes for 3D diamond
49 detectors, *Diamond and Related Materials*, Vol. 43, 23-28,2014
50
51 [12] G. Parrini, F. Fabbrizzi,, S. Lagomarsino, L. Nunziati, S. Sciortino, A. Scorzoni, Laser
52 graphitization for polarization of diamond sensors, *Proceedings of Science*, PoS(RD11)017,
53 http://pos.sissa.it/archive/conferences/143/017/RD11_017.pdf.
54
55
56 [13] Federico Picollo, Sara Gosso, Ettore Vittone, Alberto Pasquarelli, Emilio Carbone, Paolo Olivero,
57 and Valentina Carabelli , A new diamond biosensor with integrated graphitic microchannels for
58 detecting quantal exocytic events from chromaffin cells, *Advanced Materials*, 25, 34, 4696–4700, 2013
59
60
61 [14] Andrew D Greentree, Paolo Olivero, Martin Draganski, Elizabeth Trajkov, James R Rabeau,
62
63
64
65

1
2
3 Patrick Reichart, Brant C Gibson, Sergey Rubanov, Shane T Huntington, David N Jamieson, and
4 Steven Prawer, Critical components for diamond-based quantum coherent devices, *J. Phys.: Condens.*
5 *Matter* 18 S825, 2006.

6
7
8 [15] Qihong Wu, Yurong Ma, Rongchuan Fang, Yuan Liao, Qingxuan Yu, Xiangli Chen, and Kelvin
9 Wang , Femtosecond laser-induced periodic surface structure on diamond film , *Applied Physics*
10 *Letters* 82, 1703 (2003).

11
12 [16] P. Olivero, S. Rubanov, P. Reichart, S. Huntington, B. Gibson, J. Salzman, S. Prawer, D. N.
13 Jamieson, Three-Dimensional Device Fabrication in Monocrystalline Diamond Using FIB and a Novel
14 Lift-off Technique , *Microscopy and Microanalysis*, 11, S02, 856-857, (2005).

15
16
17 [17] L. Giuntini, M. Massi, and S. Calusi, "The external scanning proton microprobe of Firenze: a
18 comprehensive description," *Nucl. Instrum. Methods Phys. Res. A* 576(2-3), 266–273 (2007)

19
20
21 [18] N. Taccetti, L. Giuntini, G. Casini, A. A. Stefanini, M. Chiari, M. E. Fedi, P. A. Mandò. The pulsed
22 beam facility at the 3 MV Van de Graaff accelerator in Florence: Overview and examples of
23 applications (Conference Paper) *Nuclear Instruments and Methods in Physics Research, Section B:*
24 *Beam Interactions with Materials and Atoms.* **188** (2002) 255-260

25
26
27 [19] Maurizio Vannoni, Giuseppe Molesini, Silvio Sciortino, Stefano Lagomarsino, Paolo Olivero,
28 Interferometric characterization of mono- and polycrystalline CVD diamond, *Proc. SPIE* 7389, *Optical*
29 *Measurement Systems for Industrial Inspection VI*, 738931 (17 June 2009); doi: 10.1117/12.827535

30
31
32 [20] A. Sytchkova ; S. Lagomarsino ; M. Vannoni ; S. Calusi ; P. Olivero; Optical characterization of
33 proton irradiated diamond. *Proc. SPIE* 8167, *Optical Design and Engineering IV*, 81671O (September
34 22, 2011); doi:10.1117/12.896750.

35
36
37 [21] Stefano Lagomarsino, *Advances In Diamond-based Heterostructures*, Ph.D. Thesis in Physics,
38 Department of Physics and Astronomy of Florence, Italy, 2011.
39 http://www.infn.it/thesis/thesis_dettaglio.php?tid=6317

40
41
42 [22] S. Lagomarsino, P. Olivero, S. Calusi, D. Monticone, L. Giuntini, M. Massi, S. Sciortino, A.
43 Sytchkova, A. Sordini, and M. Vannoni, "Complex refractive index variation in proton-damaged
44 diamond," *Opt. Express* 20, 19382-19394 (2012). <http://dx.doi.org/10.1364/OE.20.019382>

45
46
47 [23] P. Olivero, S. Calusi, L. Giuntini, S. Lagomarsino, A. Lo Giudice, M. Massi, S. Sciortino, M.
48 Vannoni, E. Vittone, Controlled variation of the refractive index in ion-damaged diamond, *Diamond*
49 *and Related Materials*, Volume 19, Issues 5–6, May–June 2010, Pages 428-431, ISSN 0925-9635,
50 <http://dx.doi.org/10.1016/j.diamond.2009.12.011>.

51
52
53 [24] S. Lagomarsino, P. Olivero, F. Bosia, M. Vannoni, S. Calusi, L. Giuntini, and M. Massi , Evidence
54 of Light Guiding in Ion-Implanted Diamond , *Phys. Rev. Lett.* **105**, 233903 December 2010

55
56
57 [25] S Lagomarsino, M Bellini, C Corsi, F Gorelli, G Parrini, M Santoro, S Sciortino, Three-
58 dimensional diamond detectors: Charge collection efficiency of graphitic electrodes, *Appl. Phys. Lett.*
59 103, 233507 (2013); <http://dx.doi.org/10.1063/1.4839555>

- 1
2
3 [26] M. Massi, L. Giuntini, M. Chiari, N. Gelli, and P. A. Mandò, “The external beam microprobe
4 facility in Florence: set-up and performance,” Nucl. Instrum. Methods Phys. Res. B 190(1-4), 276–282
5 (2002).
6
7
8 [27] P. A. Mandò, “Advantages and limitations of external beams in applications to arts & archeology,
9 geology and environmental problems,” Nucl. Instrum. Methods Phys. Res. B 85(1-4), 815–823 (1994).
10
11 [28] Optical Shop Testing, Daniel Manacara ed., Wiley Interscience. 3rd edition, 2007.
12
13 [29] R. L. Hines, “Radiation Damage of Diamond by 20-keV Carbon Ions,” Phys. Rev. 138(6A),
14 A1747–A1751 (1965).
15
16 [30] A. Battiato, F. Bosia, S. Ferrari, P. Olivero, A. Sytchkova, and E. Vittone, “Spectroscopic
17 measurement of the refractive index of ion-implanted diamond,” Opt. Lett. 37(4), 671–673 (2012).
18
19 [31] K. L. Bhatia, S. Fabian, S. Kalbitzer, C. Klatt, W. Krätschmer, R. Stoll, and J. F. P. Sellschop,
20 “Optical effects in carbon-ion irradiated diamond,” Thin Solid Films 324(1-2), 11–18 (1998).
21
22 [32] A. V. Khomich, V. I. Kovalev, E. V. Zavedeev, R. A. Khmelnskiy, and A. A. Gippius,
23 “Spectroscopic ellipsometry study of buried graphitized layers in the ion-implanted diamond,”
24 Vacuum 78(2-4), 583–587 (2005).
25
26 [K] S. Praver and R. Kalish, Ion-beam-induced transformation of diamond, Phys. Rev. B 51, 15711 –
27 (1995).
28
29 [33] R. L. Hines and R. Arndt, “Radiation effects of bombardment of quartz and vitreous silica by 7.5-
30 kev to 59-kev positive ions,” Phys. Rev. 119(2), 623–633 (1960).
31
32 [34] L. Babsail, N. Hamelin, and P. D. Townsend, “Helium-ion implanted waveguides in zircon,” Nucl.
33 Instrum. Methods Phys. Res. B 59–60, 1219–1222 (1991).
34
35 [35] D. T. Y. Wei, W. W. Lee, and L. R. Bloom, “Large refractive index change induced by ion
36 implantation in lithium niobate,” Appl. Phys. Lett. 25(6), 329–331 (1974).
37
38 [36] S. Praver, R. Kalish, Ion-beam-induced transformation of diamond, Phys. Rev. B 51 15711
39 (1995).
40
41 [37] Stephanie Reich, Christian Thomsen, Raman spectroscopy of graphite, Philos. Trans. R Soc. Lond.
42 362 (November 15 2004) 2271–2288.
43
44 [38] T.V. Kononenko, V. Konov, S. Pimenov, N. Rossukanyi, A. Rukovishnikov, V. Romano, Three-
45 dimensional laser writing in diamond bulk, Diamond Relat. Mater. 20 (2011) 264–268.
46
47 [39] S. Praver, K.W. Nugent, D.N. Jamieson, J.O. Orwa, L.A. Bursill, J.L. Peng, The Raman spectrum
48 of nanocrystalline diamond, Chem. Phys. Lett. 332 (2000) 93–97.
49
50 [40] Maximilian Amsler, José A. Flores-Livas, Lauri Lehtovaara, Felix Balima, S. Alireza Ghasemi,
51 Denis Machon, Stéphane Pailhès, Alexander Willand, Damien Caliste, Silvana Botti, Alfonso San
52 Miguel, Stefan Goedecker, Miguel A.L. Marques, Crystal Structure of Cold Compressed Graphite,
53
54
55
56
57
58
59
60
61
62
63
64
65

1
2
3 Phys. Rev. Lett. 108 (2012) 065501–065504
4

5 [41] Y. Akahama, H. Kawamura, Pressure calibration of diamond anvil Raman gauge to 310 GPa, J.
6 Appl. Phys. 100 (2006) 043516.
7

8
9 [42] Laurence E. Fried, W. Michael Howard, Explicit Gibbs free energy equation of state applied to the
10 carbon phase diagram, Phys. Rev. B 61 (2000) 8734–8743.
11

12 [43] R. Kalish, T. Bernsteins, B. Shapiro & A. Talmi, A percolation theory approach to the implantation
13 induced diamond to amorphous carbon transition, Radiation Effects, 52:3-4, 153-168,
14 DOI:10.1080/00337578008210028
15
16

17 [44] Tzveta Apostolova, Stefano Lagomarsino, Silvio Sciortino, Chiara Corsi, Marco Bellini, Laser
18 irradiation of monocrystalline CVD diamond: experiment and quantum-kinetic modelling, submitted to
19 Nul. Instr. & Meth. A
20
21

22 [45] S. I. Parker, C. J. Kenney, and J. Segal, Nucl. Instrum. Methods Phys. Res. A 395, 328–343
23 (1997).
24

25 [46] S. Lagomarsino, G. Parrini, M. Bellini, C. Corsi, F. Gorelli, M. Santoro. Pulsed laser fabrication
26 of 3D Diamond detectors, Proceedings of Science, PoS(RD13)010.
27
28

29 [47] A. Oh, B. Caylar, M. Pomorski, and T. Wengler, [Diamond Relat. Mater.](#) 38, 9–13 (2013).
30
31

32 [48] S. Sciortino, S. Lagomarsino, F. Nava, Silicon carbide for high signal to noise ratio MIPs
33 detection from room temperature to 80 C, IEEE Transactions On Nuclear Science, Vol. 56, No. 4,
34 August 2009.
35
36
37
38
39
40
41
42
43
44
45
46
47
48
49
50
51
52
53
54
55
56
57
58
59
60
61
62
63
64
65